

Low-temperature, high-stress deformation of olivine under water-saturated conditions

Ikuo Katayama* and Shun-ichiro Karato

*Department of Geology and Geophysics, Yale University, New Haven, Connecticut
06520, USA*

**Present address: Department of Earth and Planetary Systems Science, Hiroshima
University, Hiroshima 739-8526, JAPAN*

Abstract

Low-temperature high-stress rheology of olivine was investigated under water-saturated conditions by large strain shear deformation experiments using the Griggs-type apparatus. Samples at $T = 1273\text{-}1373$ K and $P = 2$ GPa under water-saturated conditions deformed under a significantly lower applied stress than expected from the power-law relation and the strain rate increases more rapidly with stress. These observations suggest that an exponential flow law operates under the present experimental conditions, in which the stress dependence of activation enthalpy is characterized by the Peierls stress. The Peierls stress is determined between 1.6 and 2.9 GPa depending on the choice of the form of stress-dependence of the activation enthalpy. These values are significantly smaller than the Peierls stress under dry conditions (9.1 GPa). We suggest that water (hydrogen) incorporated in the olivine lattices decreases the Peierls stress, and hence the rate of deformation in the exponential creep is significantly enhanced by the presence of water. The reduction of the Peierls stress by water results in the highly anisotropic weakening effect of water that causes the fabric transitions in olivine. The transition between the power-law and the exponential creep occurs at relatively low stress ~ 100 MPa at a geologically relevant strain rate of 10^{-15} s $^{-1}$ when temperature is lower than 1273 K and under water-rich conditions. Hence the exponential creep might be dominated in olivine-rich rocks at low temperature and high stress under water-rich conditions, and such regions could be widespread in the subduction zone upper mantle where the cold lithospheric plates sink into the mantle.

Key words: rheology, flow law, Peierls stress, olivine, water

1. Introduction

Large extrapolation is needed in applying the laboratory data on plastic flow to geological problems and the extrapolation must be made using a flow law that is appropriate for the operating microscopic processes of deformation under given conditions. Consequently, determining the dominant deformation mechanism and an appropriate flow law formula is a key to apply the laboratory data to the geologically relevant conditions in the Earth. The most commonly used formula to analyze rheological data is the power-law formula (e.g., Frost and Ashby, 1982), viz.,

$$\dot{\varepsilon} = A\sigma^n \exp\left(-\frac{H^*}{RT}\right) \quad (1)$$

where $\dot{\varepsilon}$ is the strain rate, A is a pre-exponential factor, H^* is the activation enthalpy, R is the gas constant, T is the temperature, and σ is the stress. The physical basis of this formula is that a thermally activated process characterized by the activation enthalpy, which is independent of the stress, controls the rate of deformation. Under this assumption, the strain rate is proportional to the power of stress, but the stress and temperature dependences are separated. In addition, chemical impurities in crystals such as water are known to have large influences on the power-law creep (Carter and Avé Lallemant, 1970; Chopra and Paterson, 1984; Mei and Kohlstedt, 2000; Karato and Jung, 2003). The influence of water can be analyzed by assuming that both the pre-exponential factor A and the activation enthalpy depend on water fugacity (e.g., Karato, 2008, Chapter 10). Although some details of influence of water on the rheological properties have been analyzed for the power-law creep in olivine (e.g., Karato, 1989; Mei and Kohlstedt, 2000; Karato and Jung, 2003), not much is known about the influence of water on the exponential flow law that would dominate at high stress, low temperature conditions (e.g., Tsenn and Carter, 1987).

Under a high stress, the stress dependence of activation enthalpy becomes important and the appropriate flow becomes the exponential formula, i.e.,

$$\dot{\varepsilon} = A'\sigma^2 \exp\left(-\frac{H^*(\sigma)}{RT}\right) \quad (2)$$

where A' is a constant and $H^*(\sigma)$ is a stress-dependent activation enthalpy. In case of silicates, the stress dependence comes mostly from the stress dependence of activation enthalpy over the Peierls potential, and the activation enthalpy $H^*(\sigma)$ depends on the Peierls stress σ_p (e.g., Frost and Ashby, 1982, Chapter 2). Consequently, by analyzing the experimental data at relatively high stress conditions, one can get important information as to the nature of Peierls stress, especially the influence of water on the Peierls stress.

Therefore the purpose of the present paper is to analyze the experimental data on plastic deformation of olivine polycrystals at relatively high stress, low temperature and water-rich conditions, in order to understand how water affects the rheology of olivine in the low temperature and high stress regime (i.e., deformation by the Peierls mechanism).

2. Experimental procedure

2.1. Sample assembly

Experiments were conducted in a simple shear geometry using a Griggs-type solid medium apparatus under water-saturated conditions at temperatures of 1273-1373 K and a pressure of 2.0 GPa and strain rates ranging from 3.4×10^{-4} to $3.2 \times 10^{-5} \text{ s}^{-1}$. We used the hot-pressed olivine aggregates made from San Carlos olivine or San Carlos olivine single crystals as starting materials. The hot-pressed aggregates have grain size of $\sim 20 \text{ }\mu\text{m}$ with initially random orientations. The specimens used for the shear deformation were prepared by first drilling a cylinder of diameter 3.2 mm and then cutting off a $\sim 200 \text{ }\mu\text{m}$ thick sample slice at an angle of 45° to the long axis. The sample was then cut into half normal to the plane and a platinum strain-marker (a few μm thickness) was installed. The single crystal was prepared with the [100] parallel to the shear direction and the [001] normal to the shear plane. The olivine sample, as shown in Figure 1, was sandwiched between the alumina pistons that cut at 45° from the maximum compression direction, thus allowing a simple shear deformation. We made grooves at the interface between sample and piston to prevent slip during deformation. These materials were surrounded by a Ni capsule. Water was supplied by in-situ breakdown of a 1:7 molar mixture of talc and brucite placed next to the sample. This assembly permits only hydrogen to diffuse into the sample through the capsule. We observed nickel oxide next to the Ni metal capsule after the experiments, indicating the

oxygen fugacity was buffered by the Ni/NiO reaction. Pressure was first raised to the desired value, and then temperature was increased at a rate of ~ 30 K/min. Temperature was monitored by two Pt/Rh thermocouples placed close to the upper and lower parts of the sample. The temperature variation by two thermocouples was usually within ~ 10 - 20 K. After temperature and pressure reached the desired condition, the sample was annealed for a few hours to diffuse hydrogen homogeneously into the sample (the hydrogen diffusion length at this condition is ~ 1 mm based on Mackwell and Kohlstedt (1990)). A piston was then advanced at a constant rate using a stepping motor. The samples were quenched rapidly after experiments by switching off the thermo-controller (a few tens of seconds to room temperature) and then pressure was reduced over 3-4 hours. The shear strain was measured by the rotation of the platinum strain marker in the recovered sample (Fig. 2), which was initially oriented perpendicular to the shear direction. We also measured the sample thickness before and after experiment, and found that the sample thickness changed between 10 to 30% during experiments. We include both simple shear and compressional components of strain in our analysis assuming the Levy-von Mises formulation of non-linear rheology (e.g., Karato 2008, Chapter 3). However, the compressional effect is relatively small compared to the shear components in our large shear strain experiments ($\gamma \sim 0.6$ - 3.3). The strain rate was calculated from the obtained strain and the duration of the deformation. The samples with a small strain have relatively large errors in strain rate due to the uncertainty of the initial rotation during a loading. The experimental conditions and results are summarized in Table 1.

2.2. Water content in olivine

We measured the water content in the olivine samples after experiments using Fourier-transform infrared (FTIR) spectroscopy. The samples were prepared as a doubly polished section with a thickness of ~ 100 μm and were kept in a vacuum oven at $T = 423$ K before the measurement. The IR spectra were obtained by two hundred scans with 4 cm^{-1} resolutions using an MCT detector. The water content was calculated from the IR spectra using the calibration of Paterson (1982) as follows,

$$C_{\text{OH}} = \frac{1}{150\gamma} \int \frac{K(\nu)}{3780 - \nu} d\nu \quad (3)$$

where C_{OH} is the water concentration (ppm H/Si or ppm wt H₂O), γ is an orientation factor, and $K(\nu)$ is the absorption coefficient for a given wavenumber ν (cm⁻¹). For the polycrystalline aggregates, an orientation factor of $\gamma = 1/3$ was used. The calibration of Paterson (1982) is based on an empirical correlation between the OH stretching frequency and the absorption coefficient. Recent studies have shown that the water content in olivine becomes systematically lower when the Paterson's calibration is used (Koga et al., 2003; Bell et al., 2003) and the water content will be multiplied by a factor of ~ 3.5 if the recent calibration is applied.

2.3. Stress estimate

In a solid-medium apparatus, there is a large uncertainty in determining the differential stress using an external load-cell due to friction. Although a molten-salt assembly developed by Green and Borch (1989) has reduced the error due to friction, a systematic error is possible with this technique including the error caused by the strain-dependent friction. Furthermore, water tends to be removed from a sample to the molten salt, thus long-term deformation experiments under water-rich conditions are difficult. Therefore, we used the dislocation density of the deformed samples to infer the stress magnitude. The dislocation density of a material is uniquely related to the applied stress when deformation occurs by dislocation creep as,

$$\rho = \frac{\alpha}{b^2} \left(\frac{\sigma}{\mu} \right)^\beta \quad (4)$$

where ρ is the dislocation density, σ is the applied stress, α is a non-dimensional constant, b is the length of Burgers vector, μ is the shear modulus and β is a constant. This relation depicts a balance between the applied stress and the creation of new dislocations (e.g., Poirier, 1985), which can be applied for both the power-law and exponential creep regimes as demonstrated by Kohlstedt and Weathers (1980). Using the samples that had been deformed by the gas-medium apparatus, this relation has been well constrained ($\alpha = 10^{-2.63 \pm 0.12}$ and $\beta = 1.41 \pm 0.16$, Karato and Jung (2003)). The steady-state dislocation structures are achieved by small strain less than a few percent (Durham et al., 1977), and therefore this technique can be used for our deformed

samples. The effect of pressure on this calibration is mainly through its influence on the shear modulus (Poirier, 1985), which is less than ~4% over the pressure range used in this study. Thus the relationship between stress and dislocation density is insensitive to pressure over the range of our experiments.

The dislocation density in olivine crystals is measured in the recovered samples that are quenched rapidly after experiments (and therefore dislocations are frozen at the final stress). The samples are decorated by oxidation in air at $T = 1173$ K for ~1 hour and the oxidized dislocations are observed by back-scattered electron image using a FEG scanning electron microscope with an accelerating voltage of 15 kV and a beam current of 2.4 nA (Fig. 3). The dislocation density is estimated from the total length of dislocation in an imaged volume. The dislocation images are captured by back-scattered electron imaging technique that penetrates a depth of h from the sample surface, and therefore the dislocation length l is calculated from $l = \sqrt{l_m^2 + h^2}$, where l_m is the measured dislocation length and h is the effective thickness (for details see Karato and Lee (1999)). In this technique, uncertainties caused by the unknown orientation of dislocation line are largely eliminated and one can determine the dislocation density with high accuracy (Karato and Lee, 1999). The dislocation density in polycrystal aggregates is heterogeneous due to the crystallographic orientation and the local stress caused by the grain interactions. We therefore measured the dislocation density of total ~20 grains for each samples and the statistical average of dislocation densities was used to infer the stress magnitude. The variation of the dislocation density is shown in Figure 4, which is usually ~20-30% (Table 1). Based on the equation (5), the scatter of the dislocation density can be translated into the uncertainty in the stress estimate of ~10-20%. The calibration of dislocation density piezometer also has some uncertainties (Karato and Jung, 2003), and then total errors on the stress estimate are 15-25% (Table 1). The stress values estimated by this method correspond to the stress at the final stage of deformation. In all cases reported in this paper, deformation experiments were performed to large strains and deformation was likely at steady-state (quasi steady-state is achieved at shear strain of ~0.2-0.4 under wet conditions at similar T/T_m (Zhang et al., 2000; Jung et al., 2006)).

3. Experimental results

3.1. Deformation microstructures

The olivine samples were deformed to strains up to $\gamma = 3.3$ in a nearly simple shear geometry (compressional strain is usually less than $\sim 10\%$ of shear strain). Even in the experiments where a single crystal of olivine was used as the starting material, the samples were mostly recrystallized. The grain boundaries are almost straight or smoothly curved in the deformed samples (Fig. 3). The grain shape is nearly equant at relatively low strain but is slightly elongated at high strain. The aspect ratio (long axis/short axis) of grains is always smaller than that expected from the finite strain, suggesting the influence of dynamic recrystallization. The dislocations are mostly straight and are aligned along the [001] direction (Fig. 3), and subgrain boundaries are rare in our samples. We observed two types of lattice-preferred orientation (LPO) at different deformation conditions. At 1373 K, C-type fabric is dominated in the low stress samples, in which the [001] axis is subparallel to the shear direction and the (100) plane is subparallel to the shear plane. In contrast, B-type occurs at higher stress (> 240 MPa), showing the [001] axis subparallel to the shear direction and the (010) plane subparallel to the shear plane. At 1273 K, all samples show B-type olivine fabric at stress > 240 MPa. Detailed discussions on the olivine LPOs and the fabric transition are reported in Katayama and Karato (2006).

3.2. Water content

The IR spectra of the olivine samples show several sharp bands at 3330, 3360, 3530 and 3570 cm^{-1} (Fig. 5), related to the OH stretching vibration in olivine (Beran and Putnis, 1983; Kohlstedt et al., 1996). A broad band absorption around 3400 cm^{-1} observed in the olivine aggregates is likely due to the grain-boundary water or fluid inclusions, and we therefore subtracted the broad band from the spectra to calculate the intrinsic water content in the olivine samples. After the correction, the absorbance of the sharp bands is similar to that observed in a single crystal (Fig. 5). The water content in olivine was calculated from the sharp bands and ranges from 850 to 1100 ppm H/Si (50-65 ppm wt H_2O) based on the calibration by Paterson (1982). The estimated water contents are close to that determined under water-saturated conditions at $P = 2.0$ GPa (Kohlstedt et al., 1996; Jung et al., 2006). We analyzed several different areas of each sample and the difference in the water content is less than $\sim 20\%$. The relatively large error in the water measurement is caused by the uncertainty in defining the baseline, which can be as high as $\pm 20\%$.

3.3. Mechanical results

In order to characterize the (steady-state) rheological properties, we use the stress values estimated from the dislocation density, and the strain rate calculated from the final strain and the duration of a deformation experiment. The stress and strain rate relations of our deformed samples are shown in Figure 6. Experimental results at high temperature ($T = 1473$ K (Jung et al., 2006)) and the power-law relation of water-saturated olivine determined at higher temperature and lower stresses (Karato and Jung, 2003) are also shown in Figure 6.

A comparison with the previous results indicates that our new experimental results at low temperatures (1273 and 1373 K) and high stresses deviate significantly from the estimated values using the power-law constitutive relation. First, our data show much lower stresses than those extrapolated from the previous results using the power-law relation. Second, the strain rate depends more strongly on stress than the power-law relation with $n \sim 3$. Third, the temperature dependence of strain rate is much smaller than that of the power-law creep. All of these observations can be explained by an exponential flow law such as the one shown in equation (3) in which the activation enthalpy is reduced at high stresses. In addition, deformation microstructures also suggest that the power-law breakdown occurs in the low-temperature experiments. The olivine LPOs change from the [001](100) C-type to the [001](010) B-type with increasing stress (Katayama and Karato, 2006). However, in the power-law creep, the stress exponent is almost identical in each slip-system ($n \sim 3.5$; Bai et al., 1991), and hence the change of LPO should be insensitive to the applied stress within the power-law creep regime. In contrast, Peierls stress is sensitive to the crystal structure and consequently the stress-sensitivity can be highly anisotropic in the exponential creep regime, which is consistent with the stress sensitive fabric transition in our low-temperature experiments. We consider that these are strong evidences for the operation of an exponential flow law.

In materials with a relatively strong chemical bonding such as silicates, the most likely mechanism for the exponential flow law is the Peierls mechanism for which the constitutive relation (at high stresses) is given by equation (3) with the stress-dependent activation enthalpy, viz.,

$$\dot{\epsilon} = A' \sigma^2 \exp\left(-\frac{H_0^*}{RT} \left(1 - \left(\frac{\sigma}{\sigma_P}\right)^p\right)^q\right). \quad (5)$$

where H_0^* is the activation enthalpy at zero stress, and p and q are non-dimensional parameters that depend on the geometry of kinks (e.g., Kocks et al. (1975) Chapter 5). This equation is appropriate for *forward* motion of dislocation, and at low stresses, the influence of *backward* motion should also be included (for details see Karato (2008), Chapter 9).

Under these experimental conditions, the flow law of olivine aggregates changes from the power-law at relatively low stresses/high temperatures to the exponential flow law at relatively high stresses/low temperatures. Consequently, we inverted the data at 1273 K and 1373 K assuming the exponential flow law with the constraint that the appropriate flow law changes to the power law at 1473 K and/or at lower stresses. Following the discussion presented by Frost and Ashby (1982), we used a notion that the power-law creep and the exponential creep do not operate together and hence the total strain rate is given by

$$\dot{\epsilon} = \max\{\dot{\epsilon}_{\text{exponential creep}}, \dot{\epsilon}_{\text{power-law creep}}\}. \quad (6)$$

The strain rate for the power-law creep of wet olivine (Karato and Jung, 2003) is calculated at a given pressure and temperature, and equation (5) is used for the exponential creep.

In the exponential creep law, the activation enthalpy is reduced with the increase of applied stress, and the creep rate becomes insensitive to temperature at high stress. Consequently, the temperature dependence in the exponential flow law cannot be well constrained from the high-stress experimental data. On the other hand, the Peierls stress is well constrained by the conditions where the power-law breakdown occurs. The power-law breakdown is clearly shown in our experimental data as illustrated in the stress and temperature diagram (Fig. 7). The exponential flow law contains a large number of parameters and not all of them can be constrained from our limited data set, and therefore we tested two activation enthalpies in the analysis (300 and 518 kJ/mol) and determined a Peierls stress under the water-saturated conditions. The difference in

the activation enthalpy results in a small variation in the inferred Peierls stress as will be discussed later. Thus the data provide strong constraints on the Peierls stress but weak constraints on the activation enthalpy. The activation enthalpy is reported to be similar between the power-law and the exponential creeps for galena (Atkinson, 1976), anhydrite (Muller and Briegel, 1978) and marble (Heard and Raleigh, 1972). Therefore, in the following analysis, we used the activation enthalpy of 518 kJ/mol ($E^* = 470$ kJ/mol and $\Delta V^* = 24$ cm³/mol) that is reported for the power-law creep of wet olivine (Mei and Kohlstedt, 2000; Karato and Jung, 2003).

Although our deformed samples show two different types of LPO, the fabric strengths are relatively weak and the plastic anisotropy in olivine is generally not very strong. Wendt et al. (1998) deformed natural peridotites along two different directions (one perpendicular and another parallel to the foliation plane), and found that the sample orientation has little effect on the flow stress. In such cases, the total strength of olivine aggregates in our experimental data will not be sensitive to the different types of LPO.

The choice of p and q depends on the shape and geometry of obstacles that limit the dislocation motion. The microscopic models show that p and q should have a following range $0 < p \leq 1$, $1 \leq q \leq 2$ (Kocks et al., 1975), and therefore we analyzed our data using the various combinations of p and q within this range. The Peierls stress and a constant term A' in equation (5) were estimated by nonlinear least square fit with the different combinations of p and q . The fitting results are shown in Table 2 and illustrated in Figure 6 and 7. The Peierls stress depends on the choice of p and q , ranging 1.58 GPa to 2.87 GPa. Although the apparent activation enthalpy is assumed in this analysis ($H_0^* = 518$ kJ/mol), the lower activation enthalpy also gives similar results with less than ~10% difference in the estimate of Peierls stress ($\sigma_p = 1.59$ -2.89 GPa for $H_0^* = 300$ kJ/mol). Thus the Peierls stress is well constrained by our mechanical data of the low-temperature high-stress experiments even though the activation enthalpy is not well constrained by the limited stress range of our experiments.

The data are a little scattered from the fitting curves (Fig. 6). We consider this might be due to the indirect measurement of stress magnitude from dislocation density, which subjects to large uncertainties. We used a power-law relation of dislocation density and applied stress that was determined by Karato and Jung (2003) with a slope

of 1.4 ($\rho \propto \sigma^{1.4}$), but a slope of 2 is more frequently used (e.g., Kohlstedt et al. 1976). When a slope of 2 is used in the dislocation density versus stress relationship, then the slope in Fig. 6 becomes steeper (stress exponent is $n = 4.9$ at 1373 K, $n = 8.0$ at 1273 K). However, the primary evidence for the power-law break down is that the absolute strength values in our low temperature experiments (1273 K and 1373 K, particularly at 1273 K) are substantially smaller than those calculated from the power-law creep equation. The deviation between the extrapolated values and the actual data far exceeds the estimated errors in these measurements. For example, the discrepancy in strain rate (at 1273 K) is more than two orders of magnitude and the discrepancy in stress is about one order of magnitude. These differences are too large to be attributed to any possible errors in our measurements.

The present analysis is for the data obtained at $P = 2$ GPa for which water fugacity is ~ 12 GPa. In applying the flow law obtained here to the real Earth, a few issues need to be addressed. First, according to a theoretical model of hydrated kinks, the pre-exponential factor, A' , is likely proportional to some power of water fugacity and the zero-stress activation enthalpy corresponds to the formation (and migration) of hydrated kinks that is independent of water fugacity (Karato, 2008, Chapter 10), and consequently the flow law will have a form,

$$\dot{\epsilon} = A f_{\text{H}_2\text{O}}^r \sigma^2 \exp\left(-\frac{H_0^*}{RT} \left(1 - \left(\frac{\sigma}{\sigma_P}\right)^p\right)^q\right). \quad (7)$$

Note that both the formation enthalpy of a pair of kinks and the Peierls stress for hydrated kinks may be different from anhydrous kinks. The density and mobility of kinks are related to the chemical environments such as water fugacity, and therefore a correction should also be made for the dependence of the pre-exponential term on water fugacity.

4. Discussion

4.1. Influence of water on the Peierls stress and low-temperature plasticity of olivine

The rate of deformation of olivine aggregates under dry and wet conditions are

calculated as a function of the normalized stress and temperature at a constant strain rate (Fig. 8). In both conditions, the calculated stress in the power-law creep is lower than that of the exponential creep at high temperature, and consequently the power-law creep controls the flow of olivine aggregates at high temperatures. In contrast, at low temperatures, the stress level in the exponential creep becomes lower than that of the power-law creep. The transition occurs at around ~ 1400 K (for laboratory strain rates) in both dry and wet conditions, but the stress level at which the transition occurs is significantly lower under water-rich conditions. This is due to significant reduction of Peierls stress at the presence of water ($\sigma_{p, \text{wet}} = 2.9$ GPa) compared to that under dry conditions ($\sigma_{p, \text{dry}} = 9.1$ GPa (Evans and Goetze, 1979)). Evans and Goetze (1979) used microindentation tests on olivine single crystals, and therefore one must take care when those results are compared to our deformation experiments. The microindentation tests are insensitive to temperature and strain rate, and consequently the exponential flow law under dry conditions is not well constrained by these experiments. However, the low temperature plasticity is very sensitive to stress, and therefore parameters related to the stress sensitivity, i.e. Peierls stress, can be well constrained from the hardness tests at low temperatures. The results from conventional deformation experiments under dry conditions (Carter and AveLallemant, 1970; Blacic, 1972) are also plotted in Fig. 8, which show similar mechanical results to those determined by microindentation tests (Evans and Goetze, 1979). We therefore suggest that the Peierls stress in olivine crystal is significantly reduced by the presence of water, and that it causes significant weakening in the exponential creep regime.

The presence of water is known to enhance the dislocation climb in olivine (e.g., Karato, 1989; Yan, 1992; Mei and Kohlstedt, 2000). The influence of water on high temperature creep in olivine is usually interpreted in terms of point-defect related mechanisms (e.g., Mei and Kohlstedt, 2000; Karato and Jung, 2003). However, at low temperatures and/or high stress levels, dislocation glide may control the rate of deformation, and in this case creep rate becomes highly sensitive to the stress when stress is high enough. Our experimental results show that the water weakening is also significant in the glide-controlled exponential creep, and suggest that this is due to the decrease in the Peierls stress (Fig. 8). We note that the reduction of the Peierls stress by water also has an implication for a climb-controlled model for high temperature creep. If creep is controlled by climb of an edge dislocation under jog under-saturated

conditions, then the creep rate depends on the jog density that in turn depends on the jog formation energy that is proportional to $\sqrt{\sigma_p / \mu}$ (e.g., Hirth and Loth, 1968).

The Peierls stress is controlled by crystal structure and chemical bonding and therefore the Peierls stress in a given crystal is anisotropic. Therefore in case where the Peierls stress is reduced by the presence of water, water weakening is expected to be highly anisotropic. Although such anisotropic signature is weak in polycrystal aggregates, the change of the dominant slip system in olivine that causes the fabric transition can result from the anisotropic water weakening in the exponential creep regime (e.g., Jung and Karato, 2001; Katayama et al., 2006).

4.2. Deformation mechanisms in the subduction zone upper mantle

In order to understand the rheological behavior of olivine-rich rocks under different physical conditions, we made deformation mechanism maps based on the present experimental results combined with previous studies. Three deformation mechanisms were considered for both wet and dry conditions: (1) exponential creep; (2) power-law creep; and (3) diffusion creep. Figure 9 illustrates a map in the stress and grain size space at constant pressure (2 GPa) and temperature (1273 K). The exponential creep is dominant at high stress, the power-law creep is dominated at relatively low stress and larger grain size, and the diffusion creep is dominated at low stress and smaller grain size. The transition stress between the exponential and power-law creep is higher than 500 MPa under dry conditions, whereas it decreases significantly ~ 100 MPa under water-rich conditions. This reduction in transition stress is caused by the reduction of the Peierls stress due to the dissolution of water. The boundary between the exponential and diffusion creep regimes depends on grain size, and the transition grain size is smaller than that extrapolated from the power-law creep. The dominant deformation mechanism is also sensitive to temperature, and Figure 10 shows a deformation mechanism map as a function of stress and temperature with a given pressure (2 GPa) and grain size (1 mm). At a strain rate of 10^{-15} s^{-1} , the exponential creep is dominant at temperature less than 1000 K for both wet and dry conditions, but the stress level in which the transition occurs is lower at water-rich conditions than at dry conditions. These deformation mechanism maps suggest that the conditions where the exponential creep is dominant expands to a lower stress level in a water-rich environment, and the exponential creep might be an important mechanism at low temperature and water-rich

regions with a geologically relevant strain rate. We note that the consistency between the geological observations and the results from the extrapolation of laboratory data assuming the exponential flow law (Katayama and Karato, 2006) supports this notion. Present experiments are limited in a narrow range of pressure, but the extrapolation to high pressures can be inferred though the influence of water fugacity on the pre-exponential term and using a homologous temperature scaling law.

Our finding that water enhances the exponential flow law of olivine has important implications for understanding the dynamics of subduction zones. A large portion of subduction zone upper mantle is at relatively low temperatures and at low stress where the exponential flow law may dominate. Our results indicate that the strength of materials in these regions will be much less than the previous results under dry conditions would imply if a trace amount of water is present in these regions (see Kneller et al. (2005, 2007)). In addition, being one of the fundamental materials properties, the influence of water on the Peierls stress has important implications for a range of flow-related properties including plastic anisotropy and the microscopic mechanism for the enhancement of climb-controlled creep.

Acknowledgements

We thank Y. Nishihara, P. Skemer, S. Hier-Majumder and M. Nakada for discussions and comments, and Z. Jiang for technical assistance. Constructive comments from two anonymous reviewers helped to improve the manuscript. This study was supported in part by NSF grants (S. Karato) and by a research fellowship of the Japan society for the promotion of science (I. Katayama).

References

- Atkinson, B.K., 1976. The temperature and strain-rate dependent mechanical behavior of a polycrystalline galena ore. *Econ. Geol.* 71, 513-525.
- Bai, Q., Mackwell, S.J., Kohlstedt, D.L., 1991. High-temperature creep of olivine single crystals 1. Mechanical results for buffered samples. *J. Geophys. Res.* 96, 2441-2463.
- Bell, D.R., Rossman, G.R., Maldener, J., Endisch, D., Rauch, F., 2003. Hydroxide in olivine: A quantitative determination of the absolute amount and calibration of the IR spectrum. *J. Geophys. Res.* 108, doi10.1029/2001JB000679.

- Beran, A., Putnis, A., 1983. A model of the OH positions in olivine, derived from infrared-spectroscopic investigations. *Phys. Chem. Minerals* 9, 57-60.
- Blacic, J.D., 1972. Effect of water on the experimental deformation of olivine. In: Heard, H.C., Borg, I.Y., Carter, N.L., Raleigh, C.B. (Eds), *Fracture and Flow of Rocks*, Geophys. Monogr. pp. 109-115, AGU, Washington, D.C.
- Carter, N.L., Avé Lallemant, H.G., 1970. High temperature deformation of dunite and peridotite. *Geol. Soc. Am. Bull.* 81, 2181-2202.
- Chopra, P.N., Paterson, M.S., 1984. The role of water in the deformation of dunite. *J. Geophys. Res.* 89, 7861-7876.
- Durham, W.B., Goetze, C., Blake, B., 1977. Plastic flow of oriented single crystals of olivine 2. Observations and interpretations of the dislocation structures. *J. Geophys. Res.* 82, 5755-5770.
- Evans, B., Goetze, C., 1979. The temperature variation of hardness of olivine and its implication for polycrystalline yield stress. *J. Geophys. Res.* 84, 5505-5524.
- Frost, H.J., Ashby, M.F., 1982. *Deformation-mechanism maps: The plasticity and creep of metals and ceramics*, 166 pp., Pergamon Press.
- Goetze, C., 1978. The mechanisms of creep in olivine. *Phil. Trans. R. Soc. London, A* 288, 99-119.
- Green, H.W., Borch, R.S., 1989. A new molten salt cell for precision stress measurement at high pressure. *Eur. J. Mineral.* 1, 213-219.
- Heard, H.C., Raleigh, C.B., 1972. Steady-state flow in marble at 500° to 800°C. *Geol. Soc. Am. Bull.* 83, 935-956.
- Hirth, J.P., Loth, J., 1968. *Theory of Dislocation*, 400 pp., McGraw-Hill, New York.
- Jung, H., Karato, S., 2001. Water-induced fabric transitions in olivine. *Science* 293, 1460-1463.
- Jung, H., Katayama, I., Jiang, Z., Hiraga, T., Karato, S., 2006. Effect of water and stress on the lattice preferred orientation (LPO) in olivine. *Tectonophysics* 421, 1-22.
- Karato, S., 1989. Defects and plastic deformation of olivine. In: Karato, S., Toriumi, M. (Eds.), *Rheology of Solids and of the Earth*, pp. 176-208, Oxford Univ. Press, Oxford.
- Karato, S., 2008. *Deformation of Earth Materials*. 463 pp., Cambridge Univ. Press, New York.
- Karato, S., Lee, K.H., 1999. Stress-strain distribution in deformed olivine aggregates:

- Influence from microstructural observations and implications for texture development. In: *Proceed. Twelfth Inter. Conf. Textures of Materials*, pp. 1546-1555.
- Karato, S., Jung, H., 2003. Effects of pressure on high-temperature dislocation creep in olivine. *Phil. Mag. A* 83, 401-414.
- Katayama, I., Karato, S., 2006. Effect of temperature on the B- to C-type olivine fabric transition and implication for flow pattern in the subduction zone. *Phys. Earth Planet. Int.* 157, 33-45.
- Kocks, U.F., Argon, A.S., Ashby, M.F., 1975. Thermodynamics and kinetics of slip. *Prog. Mater. Sci.* 19, 1-291.
- Koga, K., Hauri, E., Hirschmann, M., Bell, D.R., 2003. Hydrogen concentration analyses using SIMS and FTIR: Comparison and calibration for nominally anhydrous minerals. *Geochem. Geophys. Geosys.* 4, doi:10.1029/2002GC000378.
- Kohlstedt, D.L., Goetze, C., 1974. Low-stress high-temperature creep in olivine single crystals. *J. Geophys. Res.* 79, 2045-2051.
- Kohlstedt, D.L., Goetze, C., Durham, W.B., 1976. Experimental deformation of single crystal olivine with application to flow in the mantle. In: Runcorn, S.K. (Eds.), *Petrophysics: The physics and chemistry of minerals and rocks*, pp. 35-49, John Wiley and Sons, London.
- Kohlstedt, D.L., Weathers, M.S., 1980. Deformation-induced microstructures, paleopiezometers, and differential stresses in deeply eroded fault zones. *J. Geophys. Res.* 85, 6269-6285.
- Kohlstedt, D.L., Keppler, H., Rubie, D.C., 1996. Solubility of water in the α , β and γ phases of $(\text{Mg,Fe})_2\text{SiO}_4$. *Contrib. Mineral. Petrol.* 123, 345-357.
- Kneller, E.A., van Keken, P.E., Karato, S., Park, J., 2005. B-type fabric in the mantle wedge: insights from high-resolution non-Newtonian subduction zone models. *Earth Planet. Sci. Lett.* 237, 781-797.
- Kneller, E.A., van Keken, P.E., Katayama, I., Karato, S., 2007. Stress, strain, and B-type olivine fabric in the fore-arc mantle: sensitivity tests using high-resolution steady state subduction zone models. *J. Geophys. Res.* 112, B04406, doi:10.1029/2006JB004544.
- Mackwell, S.J., Kohlstedt, D.L., 1990. Diffusion of hydrogen in olivine: Implication for water in the mantle. *J. Geophys. Res.* 95, 5079-5088.

- Mackwell, S.J., Kohlstedt, D.L., Paterson, M.S., 1985. The role of water in the deformation of olivine single crystals. *J. Geophys. Res.* 90, 11319-11333.
- Mei, S., Kohlstedt, D.L., 2000. Influence of water on plastic deformation of olivine aggregates 2. Dislocation creep regime. *J. Geophys. Res.* 105, 21471-21481.
- Muller, W.H., Briegel, U., 1978. The rheological behavior of polycrystalline anhydrite. *Eclogae Geol. Helv.* 71, 397-407.
- Paterson, M.S., 1982. The determination of hydroxyl by infrared absorption in quartz, silicate glasses and similar materials. *Bull. Mineral.* 105, 20-29.
- Poirier, J.P., 1985. *Creep of crystals*. 260 pp., Cambridge Univ. Press, New York.
- Tsenn, M.C., Carter, N.L., 1987. Upper limits of power law creep of rocks. *Tectonophysics*, 136, 1-26.
- Yan, H., 1992. Dislocation recovery in olivine. M.S. thesis, 98 pp., Univ. of Minnesota, Minneapolis.

Figure captions

Figure 1. The experimental assembly of the shear deformation experiments using a Griggs-type apparatus. The olivine samples were placed into the alumina piston, which cut at 45° from the maximum compression direction. Water was supplied by the breakdown of talc and brucite mixture at high pressure and temperature.

Figure 2. Microphotographs showing the sample deformed to large strain ($\gamma \sim 2.4$: GA-27). (A) The olivine sample is sandwiched between alumina pistons and the arrows indicate a sense of shear. (B) Enlarged image shows the Pt strain-marker and shear strain is estimated from the rotation of the strain-marker, which was originally placed normal to the shear plane.

Figure 3. (A) Dislocation microstructures of the deformed sample (GA-63) in back-scattered electron image after oxidation at 1173 K for 1 hour. The bright lines or dots within olivine grains represent dislocations. The arrows at top and bottom show a sense of shear. (B) Enlarged image showing that the dislocation is nearly straight and aligned parallel to the [001] direction.

Figure 4. Histogram of the dislocation density in the deformed sample (GA-63). The

dislocation density was measured from the back-scattered electron image of individual grains (see details in text).

Figure 5. The infrared spectrum of the deformed olivine samples (GA-27). The IR spectra of the hot-pressed starting material and the wet single crystal (Jung et al., 2006) are shown for comparison. The dotted line represents the original spectrum before a broad band subtraction. The absorption bands between 3300 and 3700 cm^{-1} correspond to the OH stretching vibration.

Figure 6. The strain rate versus stress relation of the deformed olivine samples at $T = 1273$ K and 1373 K (this study) and $T = 1473$ K (from Jung et al. (2006)) under water-saturated conditions. The shaded data are calculated with a slope of $\beta = 2$ in the dislocation density versus stress relation. The solid curves represent the fitting results of the experimental data into the flow law formula including the exponential creep and the power-law creep ($p=1$, $q=2$ are used for the exponential creep). The dashed lines indicate the power-law creep for wet olivine based on Karato and Jung (2003).

Figure 7. The creep curves of wet olivine as functions of stress and temperature at different strain rates, 10^{-3} , 10^{-4} , and 10^{-5} s^{-1} . The samples deformed at strain rates close to 10^{-4} s^{-1} are also shown as diamond symbols ($T = 1273$ K and 1373 K from this study and $T = 1473$ K from Jung et al. (2006)). The exponential creep is dominated at low temperature and high stress, whereas the power-law creep is dominated at high temperature and low stress.

Figure 8. The creep curves of wet and dry olivine as functions of normalized stress (σ/μ , μ is shear modulus) and normalized temperature (T/T_m , T_m is melting temperature), and the strain rate is normalized to 10^{-5} s^{-1} using the exponential flow law that is determined in this study. Dry data of the microindentation tests (filled diamond: Evans and Goetze (1979)) and the conventional deformation experiments (filled square: Blacic (1972), filled triangle: Carter and Avé Lallemant (1970)) are shown for comparison to the wet data (open symbol) from this study and Karato and Jung (2003). Olivine deformed at water-saturated conditions shows significantly lower flow strength than that of dry conditions in both the exponential and power-law creep regimes.

Figure 9. Deformation mechanism map of wet and dry olivine as functions of stress and grain size at $P = 2$ GPa and $T = 1273$ K. Three fields of deformation mechanism (1) exponential creep (2) power-law creep and (3) diffusion creep were computed following the Frost and Ashby (1982). The thick lines represent the transition of the deformation mechanism, and the thin lines represents constant strain rates of 10^{-5} , 10^{-10} , and 10^{-15} s $^{-1}$.

Figure 10. Deformation mechanism map of wet and dry olivine as functions of stress and temperature at $P = 2$ GPa and grain size of 1.0 mm.

Table 1. Experimental results

Sample	pressure (GPa)	temperature (K)	time (min)	compression strain	shear strain [†] (γ)	strain rate [‡] (s^{-1})	dislocation density ($\times 10^{12} m^{-2}$)	stress [§] (MPa)	water content [¶] (H/10 ⁶ Si)
GA-024*	2.0	1373	298	0.04	0.6 (± 0.4)	$3.2 (\pm 2.4) \times 10^{-5}$	1.57 (± 0.49)	172 (± 40)	860-1050
GA-027*	2.0	1373	441	0.11	2.4 (± 0.6)	$8.4 (\pm 2.1) \times 10^{-5}$	2.27 (± 0.59)	222 (± 44)	930-1160
GA-029	2.0	1373	305	0.27	2.7 (± 0.7)	$1.3 (\pm 0.3) \times 10^{-4}$	2.80 (± 0.45)	260 (± 38)	870-1120
GA-032	2.0	1373	440	0.26	1.2 (± 0.5)	$4.4 (\pm 1.8) \times 10^{-5}$	1.65 (± 0.53)	178 (± 42)	1010-1200
GA-039	2.0	1373	377	0.29	2.7 (± 0.8)	$1.0 (\pm 0.3) \times 10^{-4}$	2.55 (± 0.67)	242 (± 49)	920-1010
GA-043*	2.0	1373	161	0.13	2.0 (± 0.8)	$1.9 (\pm 0.8) \times 10^{-4}$	3.00 (± 0.68)	273 (± 49)	830-1220
GA-044*	2.0	1273	203	0.10	1.1 (± 0.5)	$8.8 (\pm 3.9) \times 10^{-5}$	3.42 (± 0.75)	299 (± 53)	850-1060
GA-061	2.0	1273	142	0.23	3.3 (± 0.9)	$3.4 (\pm 0.9) \times 10^{-4}$	4.42 (± 0.61)	360 (± 49)	820-880
GA-062	2.0	1273	290	0.20	2.7 (± 0.8)	$1.4 (\pm 0.4) \times 10^{-4}$	3.80 (± 0.60)	323 (± 47)	810-1070
GA-063	2.0	1273	1260	0.17	3.1 (± 0.7)	$3.7 (\pm 0.8) \times 10^{-5}$	2.58 (± 0.60)	245 (± 45)	960-1050

*Starting material was single crystal with the [100](001) orientation. Hot-pressed olivine aggregates were used for the other experiments.

[†]Shear strain was measured from the rotation of strain-marker. The uncertainty of the shear strain was estimated from the shape of the strain-marker and the initial rotation.

[‡]Strain rate was estimated including the compressional strain from the Levy-von Mises relations.

[§]Stress was calculated from the average of dislocation density, and the uncertainty in the stress estimate was inferred from the heterogeneity in dislocation density as well as the calibration error on the piezometer.

[¶]Water content was analyzed by FTIR after each experiment and calculated based on Paterson (1982) calibration.

Table 2. Fitting results with different choice of p and q .

	A ($\text{s}^{-1} \text{MPa}^{-2}$)	σ_p (GPa)
$p=1, q=1$	$10^{8.0 (\pm 0.5)}$	1.58 (± 0.24)
$p=3/4, q=1$	$10^{7.1 (\pm 0.6)}$	2.06 (± 0.38)
$p=1, q=4/3$	$10^{7.9 (\pm 0.5)}$	2.00 (± 0.31)
$p=3/4, q=4/3$	$10^{6.9 (\pm 0.6)}$	2.79 (± 0.55)
$p=1, q=2$	$10^{7.8 (\pm 0.6)}$	2.87 (± 0.47)

Activation enthalpy (H_0) is assumed same with the power-law.

Figure1

[Click here to download Figure\(s\): Katayama and Karato_Fig 1.pdf](#)

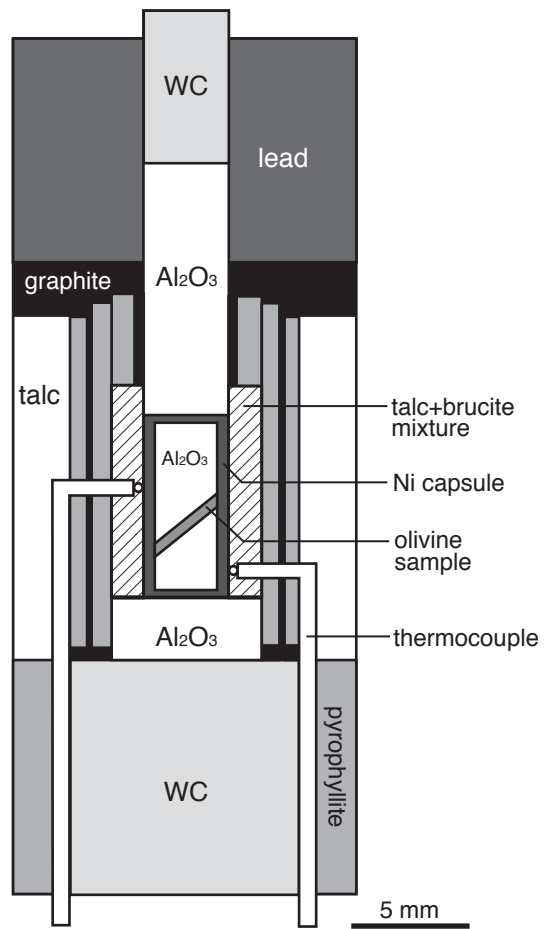


Fig. 1. Katayama and Karato

Figure2

[Click here to download Figure\(s\): Katayama and Karato_Fig 2.pdf](#)

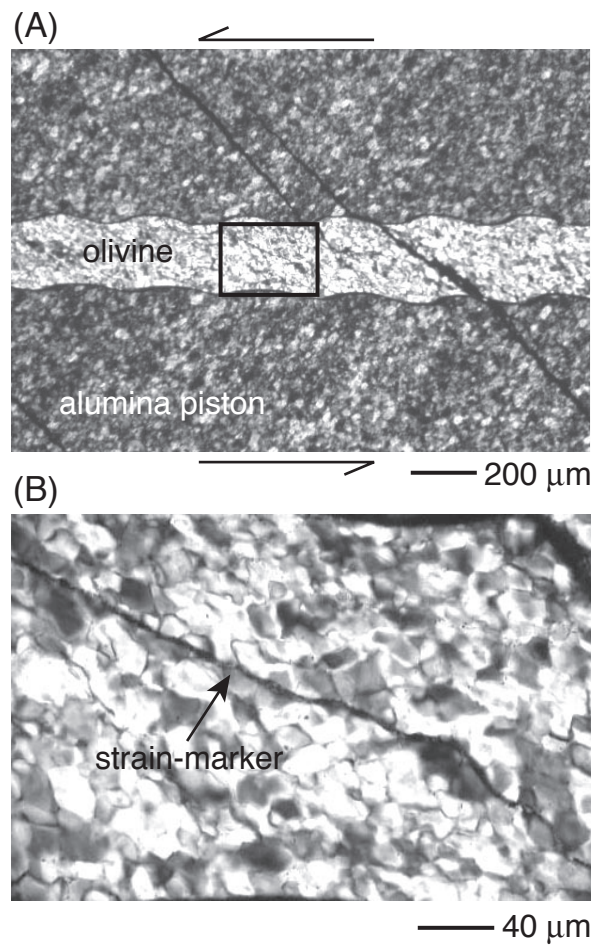


Fig. 2. Katayama and Karato

Figure3

[Click here to download Figure\(s\): Katayama and Karato_Fig 3.pdf](#)

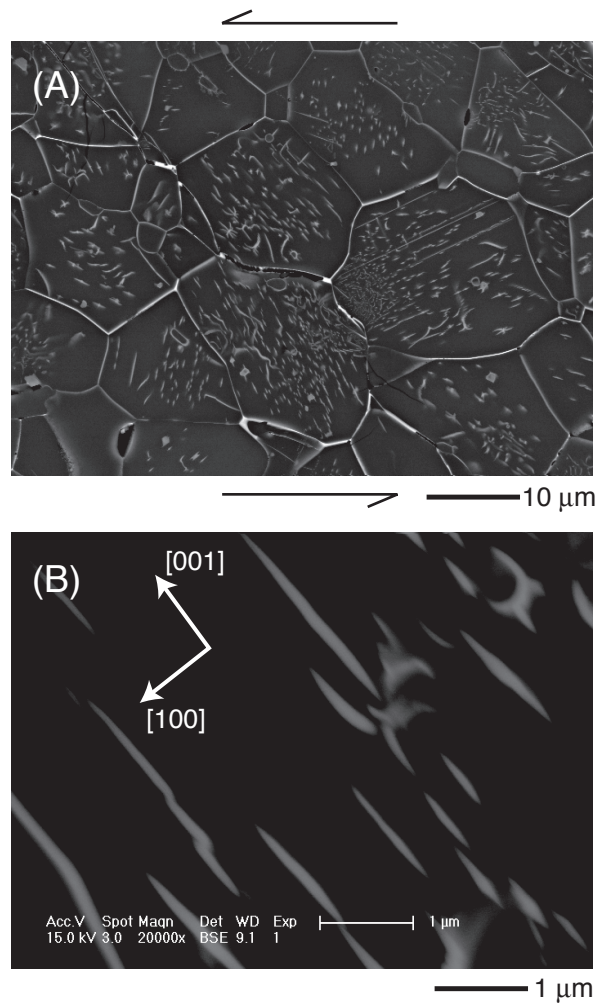


Fig. 3. Katayama and Karato

Figure4

[Click here to download Figure\(s\): Katayama and Karato_Fig 4.pdf](#)

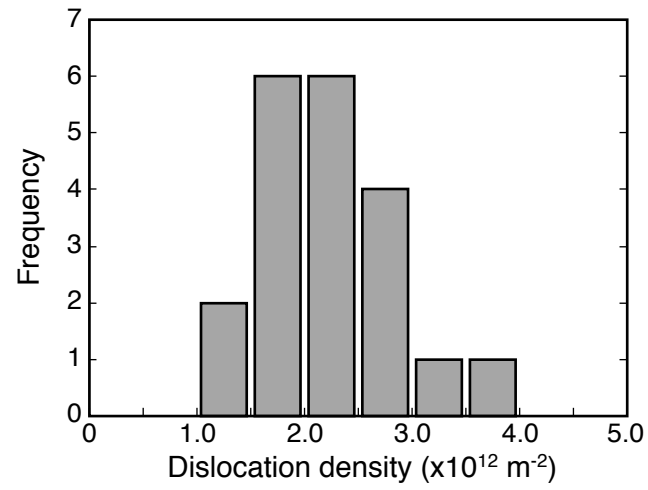


Fig. 4. Katayama and Karato

Figure5

[Click here to download Figure\(s\): Katayama and Karato_Fig 5.pdf](#)

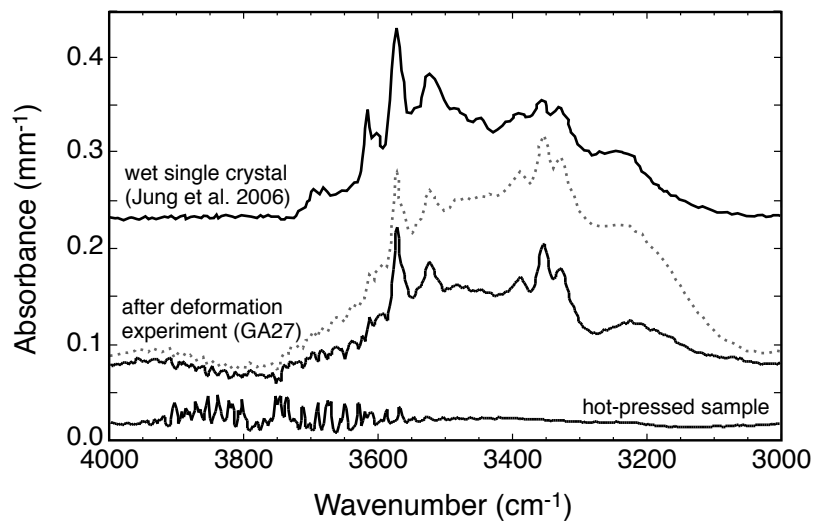


Fig. 5. Katayama and Karato

Figure6

[Click here to download Figure\(s\): Katayama and Karato_Fig 6.pdf](#)

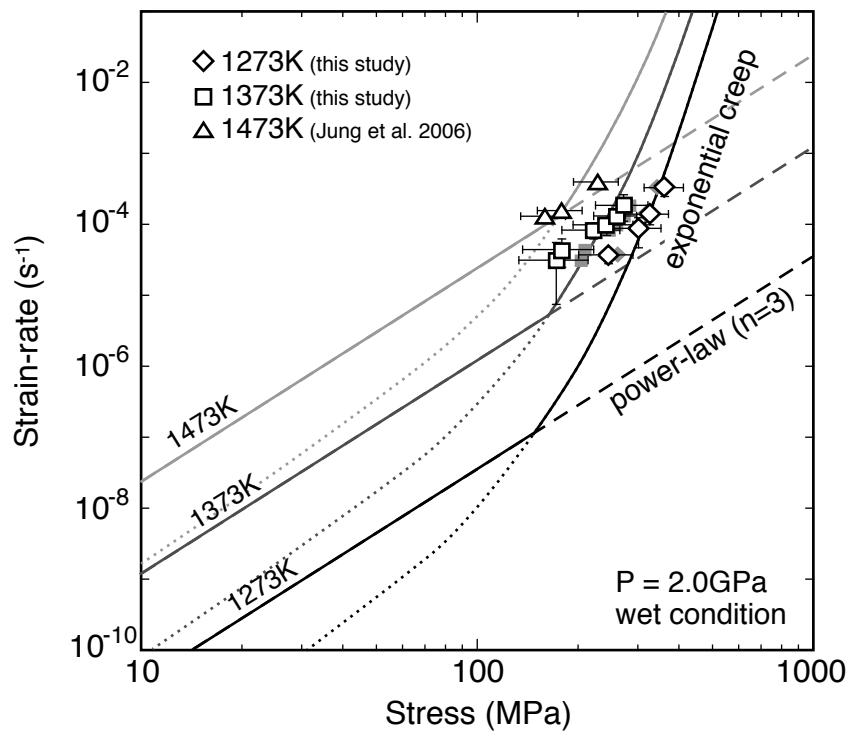


Fig. 6. Katayama and Karato

Figure7

[Click here to download Figure\(s\): Katayama and Karato_Fig 7.pdf](#)

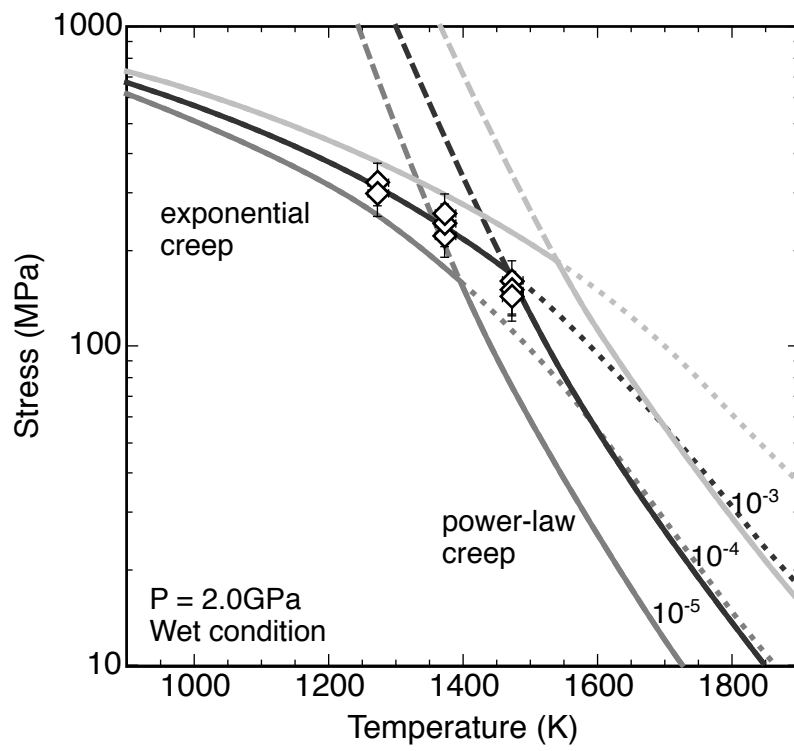


Fig. 7. Katayama and Karato

Figure8

[Click here to download Figure\(s\): Katayama and Karato_Fig 8.pdf](#)

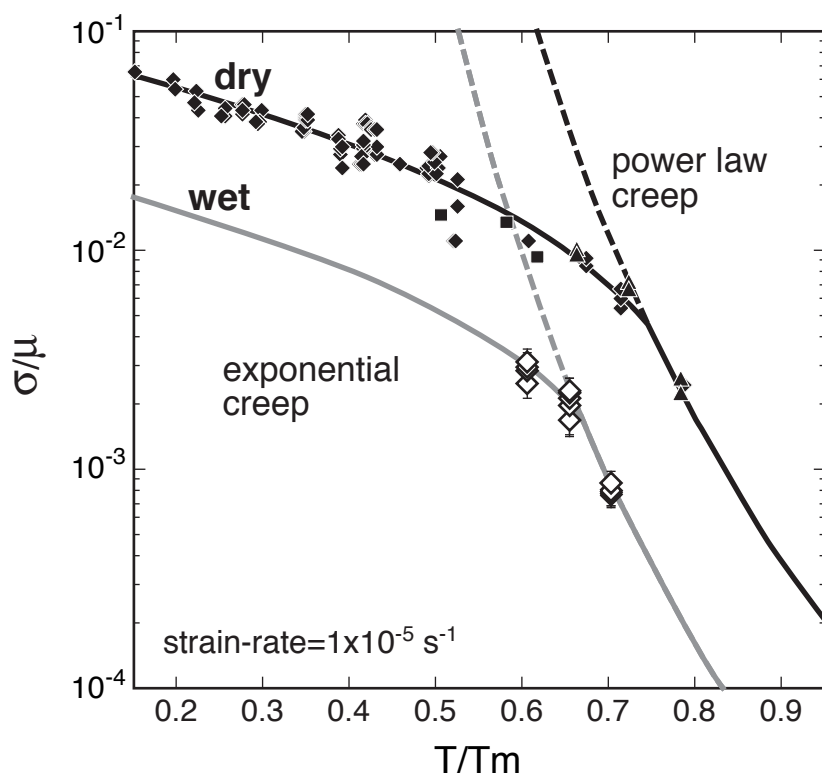


Fig. 8. Katayama and Karato

Figure9

[Click here to download Figure\(s\): Katayama and Karato_Fig 9.pdf](#)

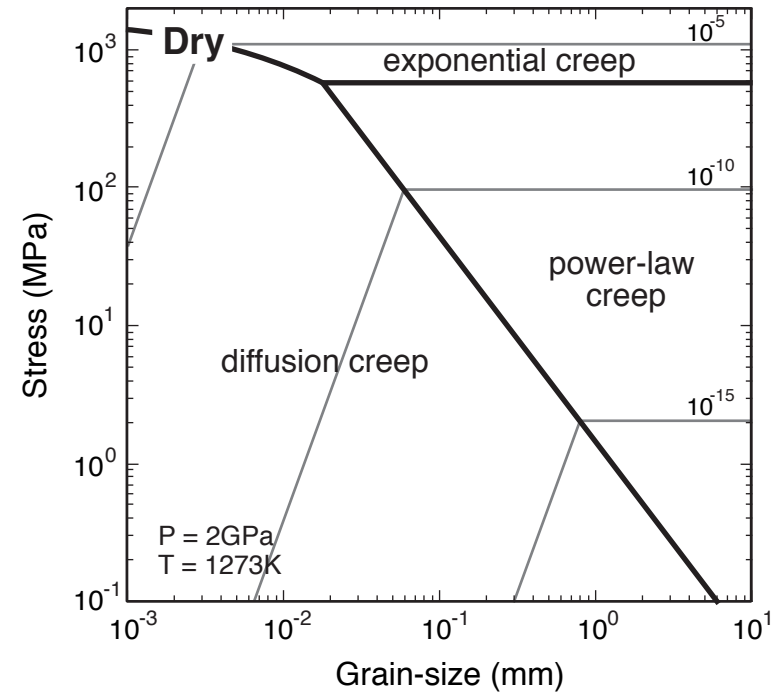
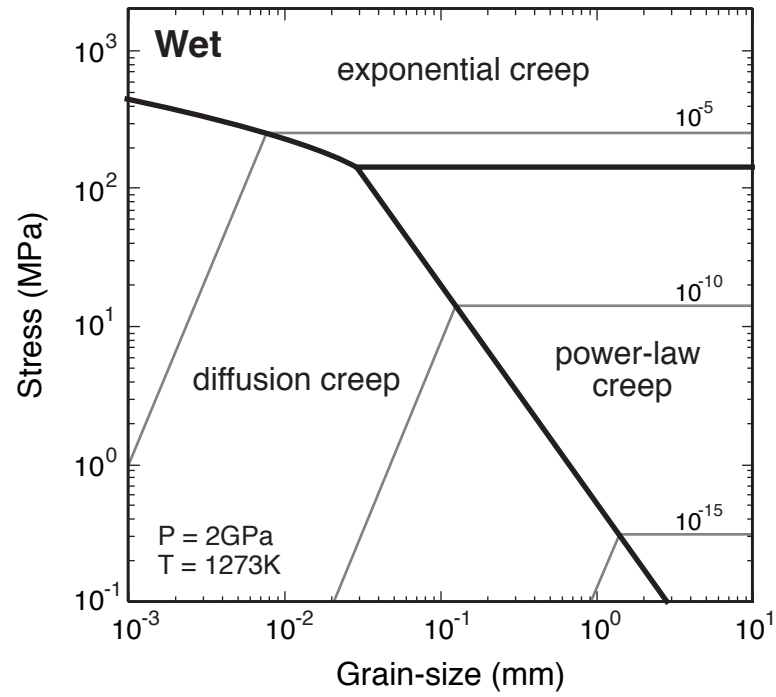


Fig. 9. Katayama and Karato

Figure10
[Click here to download Figure\(s\): Katayama and Karato_Fig 10.pdf](#)

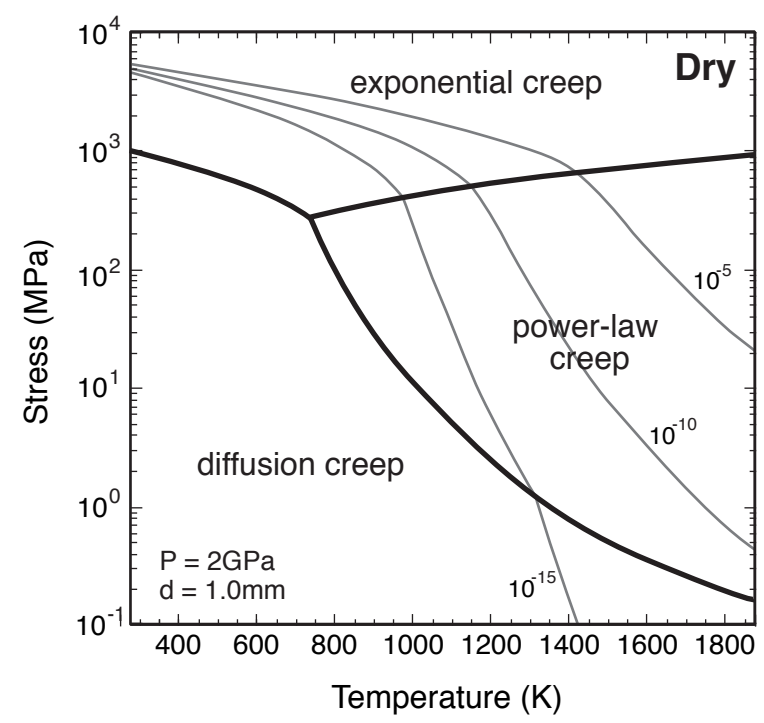
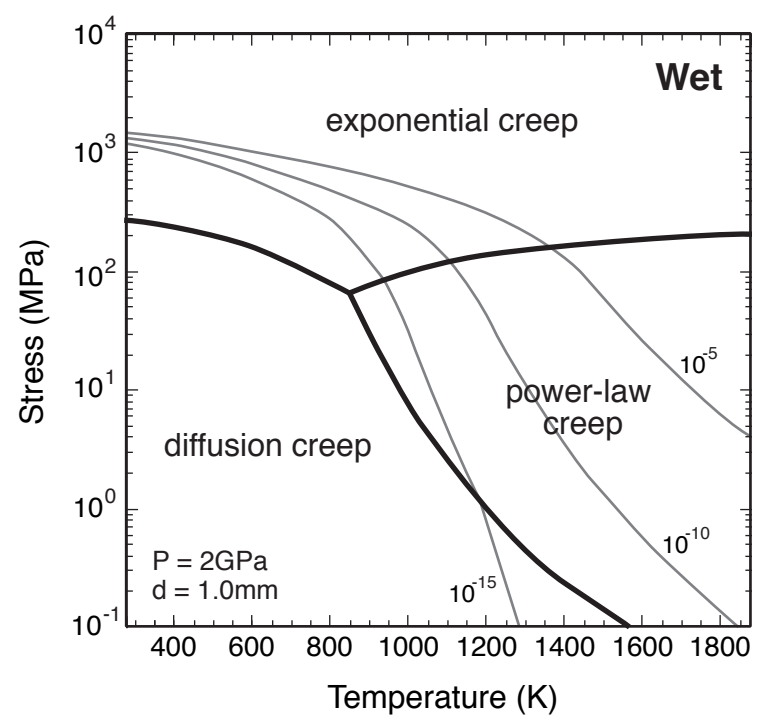


Fig. 10. Katayama and Karato